

Pattern analysis in a benthic bacteria-nutrient system

Daniel Wetzel

Institute for Mathematics

Carl von Ossietzky Universität Oldenburg, 26111 Oldenburg, Germany

d.wetzel@uni-oldenburg.de

December 3, 2024

Abstract

We study pattern formation in a reaction-diffusion system for a benthic bacteria-nutrient model in a marine sediment, which originally contains some spatially varying coefficients and with these shows some layering of patterns. Using the Landau reduction for the system with homogeneous coefficients, we locally analyze Turing bifurcations in 1D and 2D. Moreover, we use the software `pde2path` to compute the corresponding branches globally and find a number of snaking branches of patterns over patterns.

This shows that spatially varying patterns are not necessarily due to spatially varying coefficients.

Keywords: stationary fronts, localized patterns, hexagonal spots, stripes, marine sediment, bacteria-nutrient model, Landau reduction

1 Introduction

A reaction-diffusion system for a benthic bacteria-nutrient model in a marine sediment is set up and analyzed in [2]. In dimensionless form this system is described by

$$\begin{aligned}\partial_t u &= \left(\gamma + (1 - \gamma) \frac{u}{k + u} \right) u \frac{v}{1 + v} - mu + \varepsilon + \delta_u \Delta u, \\ \partial_t v &= - \left(\gamma + (1 - \gamma) \frac{u}{k + u} \right) u \frac{v}{1 + v} + \tilde{\sigma}(\tilde{y})(v_0 - v) + \delta_v \Delta v.\end{aligned}\tag{1}$$

Here $u = u(t, \tilde{x}, \tilde{y})$ denotes the population density of bacteria and $v = v(t, \tilde{x}, \tilde{y})$ the concentration of a nutrient, where \tilde{x} and \tilde{y} are the horizontal and vertical spatial coordinates in the sediment, respectively. t is the time. δ_u and δ_v are diffusion constants of bacteria and nutrient, respectively. γ describes the strength of active stimulation in a Holling II nonlinearity, k the associated half saturation constant, m the mortality of bacteria, and ε the rate of bacteria inflow, while v_0 is the nutrient concentration in the sea water above the sediment, i.e., at $\tilde{y} = 0$. The function $\tilde{\sigma}$ describes the bioirrigation.

Rescaling (1) with $x = \frac{\tilde{x}}{\sqrt{\delta_u}}$ and $y = \frac{\tilde{y}}{\sqrt{\delta_u}}$, yields

$$\begin{aligned}\partial_t u &= \left(\gamma + (1 - \gamma) \frac{u}{k + u} \right) u \frac{v}{1 + v} - mu + \varepsilon + \Delta u, \\ \partial_t v &= - \left(\gamma + (1 - \gamma) \frac{u}{k + u} \right) u \frac{v}{1 + v} + \sigma(y)(v_0 - v) + \delta \Delta v,\end{aligned}\tag{2}$$

where $\delta = \frac{\delta_v}{\delta_u} = 50$ and $\sigma(y) := \tilde{\sigma}(\tilde{y})$. In order to simplify the notation we set $w = (u, v)$, $D = \begin{pmatrix} 1 & 0 \\ 0 & \delta \end{pmatrix}$, and

$$f(u, v) = \begin{pmatrix} g(u, v) \\ h(u, v) \end{pmatrix} = \begin{pmatrix} \left(\gamma + (1 - \gamma) \frac{u}{k + u} \right) u \frac{v}{1 + v} - mu + \varepsilon \\ - \left(\gamma + (1 - \gamma) \frac{u}{k + u} \right) u \frac{v}{1 + v} + \sigma(v_0 - v) \end{pmatrix}.\tag{3}$$

The function f is called the reaction term or kinetic of the full system (2). With this simplifications we can write (2) as

$$\partial_t w = f(w) + D\Delta w. \quad (4)$$

To understand bioirrigation, we consider the system

$$\partial_t v = \sigma(v_0 - v) \quad (5)$$

for a homogeneous σ . The unique solution of (5) is given by

$$v = (v(0) - v_0)e^{-\sigma t} + v_0,$$

which converges to v_0 for $t \rightarrow \infty$. Thus the bioirrigation σ determines the speed at which the nutrient concentration in the sediment adapts to v_0 .

Here and in [2] the parameter set

$$k = 1, \quad v_0 = 4.125, \quad \varepsilon = 0.005, \quad m = 0.3175, \quad \delta_u = 2 \cdot 10^{-5}, \quad \delta_v = 10^{-3} \quad (6)$$

is used and spot patterns are classified in cold and hot, which means that they have a minimum and maximum in the center of every spot, respectively. Because of the predator prey structure of (1) we have a hot-spot pattern for u , when we have a cold-spot pattern for v and vice versa. Thus we always present only the pattern of u , and when we are saying that a solution of (1) is hot or cold, this means that this is the case for u .

For homogeneous bioirrigations and $\gamma = 0.25$ stable solutions with the following patterns are found in [2] via time-integrations: A homogeneous pattern with a low density of bacteria for $\sigma = 0.05$, hexagonal hot-spots for $\sigma = 0.08$, stripes for $\sigma = 0.1$, hexagonal cold-spots for $\sigma = 0.125$, and a homogeneous pattern with a high density of bacteria for $\sigma = 0.14$ (see Fig.10 of [2]). Furthermore, the system (1) is studied in [2] for depth-dependent bioirrigation functions of the form

$$\bar{\sigma}(\tilde{y}) = \alpha e^{(-\tilde{y}/\mu)}.$$

Quasi-stationary layering of patterns involving stripes and hot spots are observed for $\mu = 10$, $\gamma = 0.25$, and $\alpha = 0.1$ (see Fig.11 of [2]). By changing the diffusion constant δ_x to $7 \cdot 10^{-6}$ and using $\mu = 3$, $\gamma = 0.25$, and $\sigma = 0.2$, a quasi-stationary solution is found, which involves three different types of patterns. These are homogeneous, cold-spot, and stripe patterns (see Fig.12 of [2]). Here we describe the bioirrigation by

$$\sigma(y) = \frac{0.128}{1 + e^{0.011(y-480)}} \quad (7)$$

and obtain a quasi-stationary solution involving all five pattern types shown in Fig.10 of [2] (see Fig.1). Using the Landau analysis described below, we predict a transition of stability between cold spots and stripes and between stripes and hot spots in the ranges $y \in [265, 296]$ and $y \in [380, 418]$, respectively. One can see in Fig.1 that this is a sensible prediction.

The goal of this paper is to continue the investigations of [2] by understanding the bifurcation scenarios of (1) for homogeneous bioirrigations and to find and investigate more stationary patterns via bifurcation analysis. Mostly we see γ as a given and fixed parameter, while we use σ as a bifurcation parameter, i.e., we examine how solutions and their types of stability change and what kind of new solutions bifurcate by varying σ .

It is shown in [2] that the problem of determining the homogeneous solutions can be reduced to computing the zeros of a cubic polynomial. The coefficients are given with some typos. The first γ of a_1 must be σ . The zeros of this polynomial are not derived analytically in [2] because of their complex terms. In Section 2 we show the reduction to the cubic polynomial again and sort the coefficients with respect to σ and γ , because we investigate (1) in the following for different values of σ and γ , while we use the set (6) for all other parameters of (1). Furthermore, we apply analytical formulas for the three zeros of the cubic polynomial to determine the regions of a bounded domain of the σ - γ -plane, where the homogeneous solutions are real and to see for

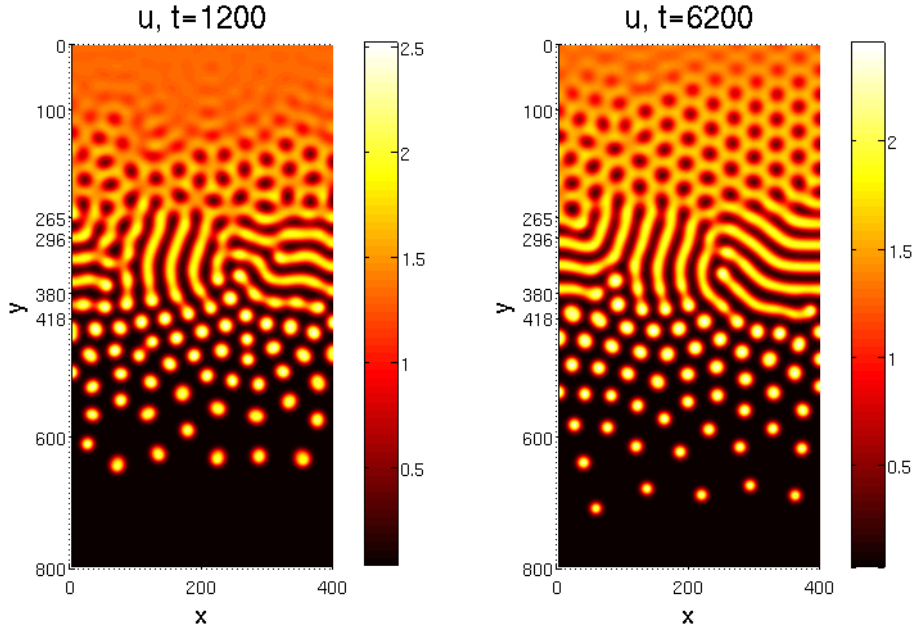


Figure 1: Density plots of u at times $t = 1200$ and 6200 , which we found by using time-integration methods for a small random perturbation of $(u, v) \equiv (1, 1)$. Here we use (2) for $\gamma = 0.25$ and $\delta = 50$. The bioirrigation is described by (7).

which combinations of σ and γ exist only one or rather three homogeneous states. It follows an introduction of Turing-instabilities and bifurcations. By using a fine discretization of the σ - γ -domain, we determine Turing unstable ranges. With this information we are able to predict the bifurcation locations and wavenumbers of periodic 1D and 2D solutions.

In Section 3 we recall how to reduce a general two species reaction-diffusion system to the Landau amplitude equation system on a hexagonal lattice. The Landau reduction can be used to approximate solutions and develop bifurcation diagrams, but this only works close to the bifurcation from the homogeneous solution. Hence, we use the continuation and bifurcation software `pde2path` [23] to get a global picture.

In Section 4 we study non trivial patterns over 1D domains and show global bifurcation diagrams for $\gamma = 0.3$, which we developed by using `pde2path`. We find that some stripe solutions bifurcate from the homogeneous branch and terminate in a different bifurcation on the homogeneous branch by holding their wavelength. Moreover, we find stripe branches of the same wavelength which are not connected, but change their wavelength and connect to other stripe branches. Using the Landau reduction, we choose a γ -value where stripes bifurcate subcritically, to develop bifurcation diagrams with snaking branches of localized stripes on homogeneous backgrounds.

In Section 5 we investigate 2D patterns and develop some global bifurcation diagrams by using `pde2path`. Furthermore, we show solutions and solution branches of localized hexagonal spots with a planar interface to striped backgrounds and patches of localized hexagons on homogeneous backgrounds. The patches which we find first have a flat overlying front such that the snake does not show a strong snaking behavior. Hence, we use the Landau reduction to find γ -values where the front is steeper and thus the snaking behavior is more pronounced. We end in Section 6 with a discussion and an outlook.

From this we see that a layering of patterns is not necessarily an effect of space dependent parameters but can occur for homogeneous bioirrigations. A bifurcation analysis for depth dependent functions will be presented elsewhere.

Acknowledgement. I am indebted to U. Feudel and H. Uecker for stimulating and enlightening discussions.

2 Homogeneous solutions and Turing instabilities

Homogeneous steady states are solutions of $f(u, v) = 0$ which are space and time independent. For a nonzero rate of bacteria inflow ε and nonzero product of the bioirrigation σ and the nutrient concentration v_0 in the sea water it holds

$$u \neq 0, \quad v \neq 0 \quad (8)$$

for homogeneous solutions of (2). Adding the first to the second equation of (3), yields the linear relationship

$$v = v_0 - \frac{mu - \varepsilon}{\sigma}. \quad (9)$$

From (8), (9), and the fact that the population density of the bacteria u and the concentration of the nutrient v cannot be smaller than zero follows

$$u \in \left(0, \frac{\varepsilon + \sigma v_0}{m}\right), \quad v \in \left(0, v_0 + \frac{\varepsilon}{\sigma}\right).$$

Substituting (9) into $f(u, v) = 0$, reduces the problem to

$$u^3 + bu^2 + cu + d = 0 \quad (10)$$

with

$$b = b_g\gamma + b_s\sigma + b_0, \quad c = c_g\gamma + c_s\sigma + c_{sg}\sigma\gamma + c_0, \quad d = d_s\sigma + d_0,$$

where

$$\begin{aligned} b_g &= -\frac{k}{m-1} \approx 1.47, & b_s &= \frac{v_0 - v_0m - m}{m(m-1)} \approx -11.53, & b_0 &= \frac{m^2k + \varepsilon - 2m\varepsilon}{m(m-1)} \approx -0.47, \\ c_g &= \frac{\varepsilon k}{m(m-1)} \approx -0.02, & c_s &= \frac{(v_0 + 1)(\varepsilon - mk)}{m(m-1)} \approx 7.39, & c_{sg} &= \frac{v_0k}{m(m-1)} \approx -19.04, \\ c_0 &= \frac{-2m\varepsilon k + \varepsilon^2}{m(m-1)} \approx 0.01, & d_s &= \frac{\varepsilon k(v_0 + 1)}{m(m-1)} \approx -0.12, & d_0 &= \frac{\varepsilon^2 k}{m(m-1)} \approx -10^{-4}. \end{aligned}$$

The zeros of (10) are given by

$$\begin{aligned} u_1 &= \sqrt{-\frac{4p}{3}} \cos\left(\frac{1}{3} \arccos\left(-\frac{q}{2} \sqrt{-\frac{27}{p^3}}\right)\right) - \frac{b}{3}, \\ u_2 &= -\sqrt{-\frac{4p}{3}} \cos\left(\frac{1}{3} \arccos\left(-\frac{q}{2} \sqrt{-\frac{27}{p^3}}\right) + \frac{\pi}{3}\right) - \frac{b}{3}, \\ u_3 &= -\sqrt{-\frac{4p}{3}} \cos\left(\frac{1}{3} \arccos\left(-\frac{q}{2} \sqrt{-\frac{27}{p^3}}\right) - \frac{\pi}{3}\right) - \frac{b}{3}, \end{aligned}$$

where

$$p = c - \frac{b^2}{3}, \quad q = \frac{2b^3}{27} + d - \frac{bc}{3}.$$

The polynomial (10) can have one or three real zeros for fixed σ and γ . The regions of the σ - γ -plain, where a homogeneous solution is real, can be calculated analytically. Determining analytically, where the population density of the bacteria and the nutrient concentration of such a solution is additionally positive, seems not so trivial. In Fig.2(a) we show the regions on a bounded domain of the σ - γ -plain, where homogeneous solutions are real. They are also positive for the regions shown in Fig.2(b). Comparing (a) and (b), we see that the positivity is not fulfilled for all homogeneous solutions (u, v) of (10). Here (u_2, u_3) and (v_1, v_2) are negative in the upper horizontal gray band and the lower left gray region of Fig.2a), respectively.

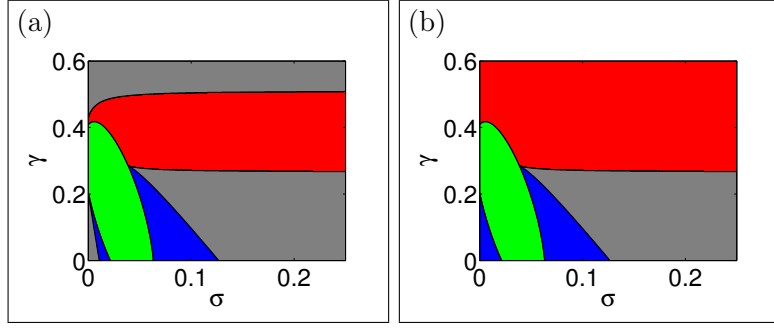


Figure 2: (a) (u_1, v_1) , (u_2, v_2) , and (u_3, v_3) are real in red, green, and blue regions, respectively. All three are real in the gray regions. This also holds for (b), where, in addition, the three homogeneous states are positive in the gray regions. To perform these figures, we discretize the σ - γ -domain $(0, 0.25) \times (0, 0.6)$ in 1000×1000 points and prove for every point the corresponding conditions.

We verified that the conditions

$$u_1 > u_2 > u_3 \quad \text{and} \quad v_1 < v_2 < v_3$$

hold for all discretization points used to generate Fig.2, if all three homogeneous states are real. Thus (u_1, v_1) is the state with the highest population density of bacteria and lowest concentration of nutrient of these three homogeneous states, while this is the opposite case for (u_3, v_3) . The equilibrium (u_2, v_2) lies in the middle.

The Jacobian of f is given by

$$J_f(u, v) = \begin{pmatrix} g_u & g_v \\ h_u & h_v \end{pmatrix} = \begin{pmatrix} \xi - m & \vartheta \\ -\xi & -\vartheta - \sigma \end{pmatrix},$$

where

$$\xi = \left(\gamma + (1 - \gamma) \frac{2ku + u^2}{(k + u)^2} \right) \frac{v}{1 + v}, \quad \vartheta = \left(\gamma + (1 + \gamma) \frac{u}{k + u} \right) \frac{u}{(1 + v)^2}.$$

The linearization of (4) in a homogeneous state w^* is given by the linear operator $L(\Delta) = J_f + D\Delta$. It holds

$$L(\Delta)e^{i(x,y) \cdot \mathbf{k}} = \hat{L}(|\mathbf{k}|)e^{i(x,y) \cdot \mathbf{k}} \quad \text{with} \quad \hat{L}(|\mathbf{k}|) = J_f - D|\mathbf{k}|^2 \quad \text{and} \quad \mathbf{k} \in \mathbb{R}^2.$$

This yields the eigenvalue problem

$$\hat{L}(|\mathbf{k}|)\phi(|\mathbf{k}|) = \mu(|\mathbf{k}|)\phi(|\mathbf{k}|), \quad (11)$$

where

$$\mu_{\pm}(|\mathbf{k}|) = \frac{\text{tr}\hat{L}(|\mathbf{k}|)}{2} \pm \sqrt{\left(\frac{\text{tr}\hat{L}(|\mathbf{k}|)}{2} \right)^2 - \det\hat{L}(|\mathbf{k}|)}. \quad (12)$$

The homogeneous solution w^* is called Turing-unstable, if the following two conditions are fulfilled:

- i) w^* is linear stable in the reaction-system, i.e., $\text{Re}[\mu_+(0)] < 0$ and $\text{Re}[\mu_-(0)] < 0$.
- ii) w^* is linear unstable in the full system (4), i.e., it exists a \mathbf{k} such that $\text{Re}[\mu_+(|\mathbf{k}|)] > 0$ or $\text{Re}[\mu_-(|\mathbf{k}|)] > 0$.

Let

$$b_1 = -g_u - h_v, \quad b_2 = g_u h_v - g_v h_u, \quad b_3 = dg_u + h_v, \quad b_4 = (\delta g_u + h_v)^2 - 4\delta(g_u h_v - g_v h_u).$$

It can be shown (see [20]) that a homogeneous state of (4) is

- stable, if $b_1 > 0 \wedge b_2 > 0 \wedge (b_3 < 0 \vee b_4 < 0)$, (13)

- unstable, if $b_1 < 0 \vee b_2 < 0$, (14)

- Turing unstable, if $b_1 > 0 \wedge b_2 > 0 \wedge b_3 > 0 \wedge b_4 > 0$. (15)

We call a solution a Turing endpoint and Turing bifurcation point, if it lies at a transition from Turing-unstable to unstable and from Turing-unstable to stable, respectively. Turing bifurcation points occur, if $\det \hat{L}(|\mathbf{k}|)$ vanishes. We call the corresponding σ and $|\mathbf{k}|$ critical bioirrigation σ_c and critical wavenumber k_c , respectively.

In Fig.3 we illustrate the stabilities of the three different homogeneous states in the σ - γ -domain of Fig.2. First of all we can see in Fig.3(c) that (u_3, v_3) is always stable, if it is real in our chosen region. By using the strength of bioirrigation σ as bifurcation parameter and the activity stimulation γ as a fixed parameter, we can classify the bifurcation scenarios into five different types. We do this by partitioning the γ -interval into the following five sections

$$I_1 = (0, 0.14], \quad I_2 = (0.14, 0.28], \quad I_3 = (0.28, 0.34], \quad I_4 = (0.34, 0.47], \quad I_5 = (0.47, 0.6].$$

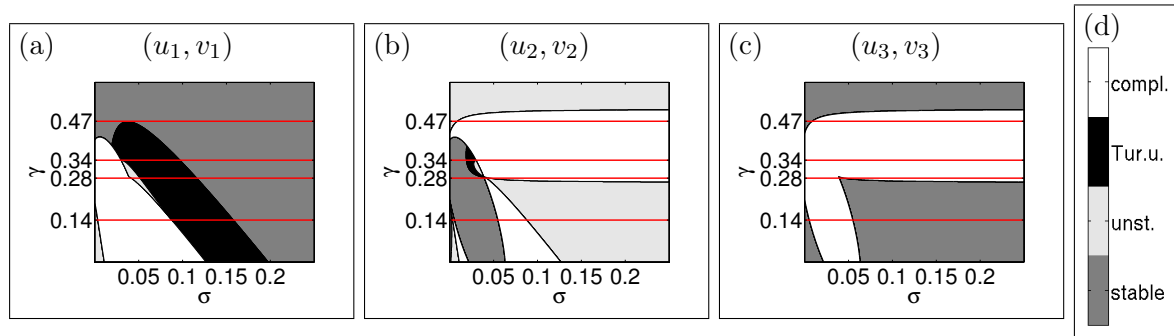


Figure 3: Illustrated are the stabilities for (u_1, v_1) , (u_2, v_2) , and (u_3, v_3) in (a), (b), and (c), respectively. We use the same σ - γ -domain and discretization like in Fig.2 to prove the corresponding conditions (13), (14), and (15). The red lines are the boundaries of the intervals I_1 , I_2 , I_3 , I_4 , and I_5 . The color bar for (a), (b), and (c) is shown in (d). The abbreviations compl., Tur.u., and unst. stand for complex, Turing-unstable, and unstable, respectively.

The least interesting interval is I_5 . Here the state (u_1, v_1) is always real, positive, and stable, while the other two are not real or not positive. For all other intervals we have Turing-unstable ranges with Turing bifurcation points at the right boundaries. The different behaviors at the left boundaries and what happens beyond is as follows.

I_1 : (u_1, v_1) equals (u_2, v_2) , stops to be real, and a fold occurs. The branch continues on (u_2, v_2) and is unstable.

I_2 : (u_1, v_1) becomes unstable (Turing endpoint) before following the behavior of I_1 .

For I_3 and I_4 there is always only one real homogeneous state, which is also positive. By increasing σ from 0 to 0.25, the stability of this state changes for the different intervals as follows:

I_3 : stable \rightarrow Turing-unstable \rightarrow unstable \rightarrow Turing-unstable \rightarrow stable

I_4 : stable \rightarrow Turing-unstable \rightarrow stable

Thus for I_4 we have one Turing unstable range, which ends up with Turing bifurcation points, while the Turing unstable range is non-contiguous for I_3 . Here we have two Turing bifurcation points and two Turing end points.

Turing patterns branch from Turing bifurcation points as discussed below. It is unclear for us which kind of solutions bifurcate from Turing endpoints. Here we have $\text{Re}[\mu_{\pm}(0)] = 0$, while $\text{Im}[\mu_{\pm}(0)] \neq 0$ such that we have Hopf bifurcations at the Turing endpoints. Currently `pde2path` [23] does not handle Hopf bifurcations and thus we postpone this analysis.

Example bifurcation diagrams for I_1 and I_3 can be seen in Fig.3 (a) and (d), respectively. Fig.3 (c) and (d) show diagrams for I_2 . In (d) we can see that (u_2, v_2) connects to (u_3, v_3) .

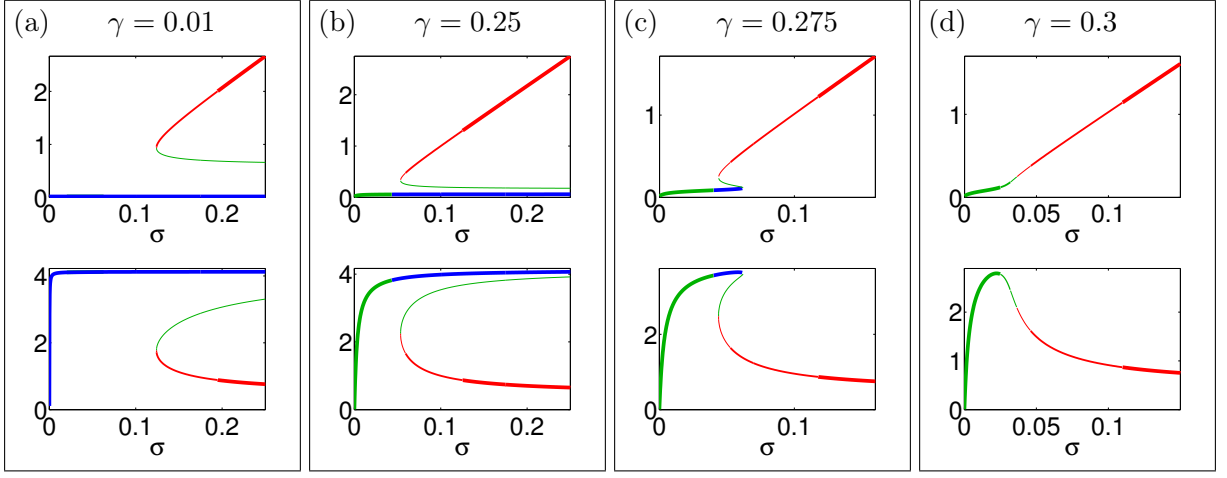


Figure 4: Shown are the bifurcation diagrams of homogeneous positive real solutions for $\gamma = 0.01, 0.25, 0.275,$ and 0.3 in (a), (b), (c), and (d), respectively. Red, green, and blue lines represent $u_1, u_2,$ and u_3 in the upper diagrams and $v_1, v_2,$ and v_3 in the lower ones, respectively. Thick, medium, and thin lines represent stable, Turing-unstable, and unstable solutions, respectively.

3 Landau reduction

First we recall how the Landau reduction works in general for systems of the form (4).

Let $w^* = (u^*, v^*)$ be a homogeneous solution of f and i, j two non-negative integers. We write $\partial_u^i \partial_v^j f(w^*)$ as $\underbrace{f u \dots u}_{i \text{ times}} \underbrace{v \dots v}_{j \text{ times}}$. We use an analog notation for g and h . Taylor-expanding f around (u^*, v^*) to third order and setting $w = (\tilde{u}, \tilde{v}) = (u, v) - (u^*, v^*)$, we obtain

$$\begin{aligned}
 f(w) &\approx \sum_{\substack{a, b \in \mathbb{N}_0 \\ a+b \leq 3}} \partial_u^a \partial_v^b f(w^*) \frac{\tilde{u}^a \tilde{v}^b}{a! b!} \\
 &= \underbrace{f_u \tilde{u} + f_v \tilde{v}}_{J_f(w^*) w^T} + \frac{1}{2} f_{uu} \tilde{u}^2 + f_{uv} \tilde{u} \tilde{v} + \frac{1}{2} f_{vv} \tilde{v}^2 + \frac{1}{6} (f_{uuu} \tilde{u}^3 + f_{vvv} \tilde{v}^3) + \frac{1}{2} (f_{uuv} \tilde{u}^2 \tilde{v} + f_{uvv} \tilde{u} \tilde{v}^2).
 \end{aligned}$$

We stop at order three, because we also use the Landau reduction only up to third order. Substituting the expansion above into (2), the system becomes

$$\partial_t w = L(\Delta)w + B(w, w) + C(w, w, w), \quad (16)$$

where $L(\Delta) = J_f(w^*) + \begin{pmatrix} \Delta & 0 \\ 0 & d\Delta \end{pmatrix}$. B and C are symmetric bilinear and trilinear forms, respectively. For $p, q, r \in \mathbb{R}^2$ they have the form:

$$\begin{aligned}
 B(p, q) &= \frac{1}{2} f_{uv} (p_1 q_2 + p_2 q_1) + \frac{1}{2} (f_{uu} p_1 q_1 + f_{vv} p_2 q_2), \\
 C(p, q, r) &= \frac{1}{6} (f_{uuu} p_1 q_1 r_1 + f_{vvv} p_2 q_2 r_2) \\
 &\quad + \frac{1}{6} (f_{uuv} (p_1 q_1 r_2 + r_1 p_1 q_2 + q_1 r_1 p_2) + f_{uvv} (p_1 q_2 r_2 + r_1 p_2 q_2 + q_1 r_2 p_2)).
 \end{aligned}$$

The eigenvalue μ_- is negative in Turing-unstable ranges, while the eigenvalue μ_+ has positive parts. Thus we always consider μ_+ in the following and write μ for simplicity.

The spot patterns shown in Fig.1 and [2] have a hexagonal structure, because every spot has six direct neighbors. Thus we start our Landau reduction on hexagonal lattices with the following ansatz

$$w = \sum_{i=1}^3 A_i e_i \Phi + c.c. = (A_1 e_1 + A_2 e_2 + A_3 e_3) \Phi + c.c. \quad (17)$$

to reduce (16) to a system of space-independent amplitudes. Here $\Phi = \phi(k)$ is the eigenvector of $\hat{L}(k)$, $e_j = e^{i(x,y) \cdot \mathbf{k}_j}$, $A_j = A_j(t) \in \mathbb{C}$ for $j = 1, 2, 3$,

$$\mathbf{k}_1 = k \begin{pmatrix} 1 \\ 0 \end{pmatrix}, \quad \mathbf{k}_2 = \frac{k}{2} \begin{pmatrix} -1 \\ \sqrt{3} \end{pmatrix}, \quad \text{and} \quad \mathbf{k}_3 = \frac{k}{2} \begin{pmatrix} -1 \\ -\sqrt{3} \end{pmatrix}.$$

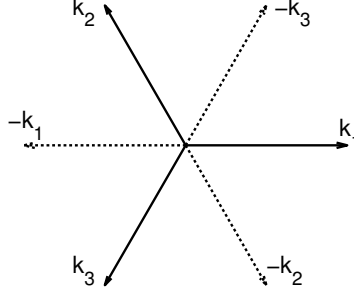


Figure 5: Sketch of the vectors k_1 , k_2 , k_3 .

The length (wavenumber k) of the wave vectors \mathbf{k}_1 , \mathbf{k}_2 , \mathbf{k}_3 is chosen such that there is a bifurcation parameter value σ_k for which the curve of eigenvalues has a zero in k . It holds

$$\partial_t w = \sum_{i=1}^3 \partial_t A_i e_i \Phi + c.c., \quad L(\Delta)w = \mu(k) \sum_{i=1}^3 A_i e_i \Phi + c.c.,$$

$$\begin{aligned} B(w, w) = & \left(\left(\sum_{i=1}^3 A_i^2 e_i^2 \right) B(\Phi, \Phi) + (2\overline{A_1 A_2} e_3 + 2\overline{A_1 A_3} e_2 + 2\overline{A_2 A_3} e_1) B(\Phi, \overline{\Phi}) \right. \\ & \left. + \left(\sum_{i=1}^3 |A_i|^2 + \sum_{1 \leq i < j \leq 3} 2A_i \overline{A_j} e_i \overline{e_j} \right) B(\Phi, \overline{\Phi}) \right) + c.c., \end{aligned}$$

and

$$\begin{aligned} C(w, w, w) = & \left((A_1 e_1 + A_2 e_2 + A_3 e_3)^3 C(\Phi, \Phi, \Phi) \right. \\ & \left. + 3(A_1 e_1 + A_2 e_2 + A_3 e_3) (\overline{A_1 e_1 + A_2 e_2 + A_3 e_3})^2 C(\Phi, \overline{\Phi}, \overline{\Phi}) \right) + c.c.. \end{aligned}$$

To eliminate quadratic terms from the residual $\text{Res}(w) = -\partial_t w + L(\Delta)w + B(w, w) + C(w, w, w)$ which do not correspond to modes e_1 , e_2 , or e_3 , we extend the ansatz (17) to

$$w = \sum_{i=1}^3 A_i e_i \Phi + \left(\sum_{i=1}^3 A_i^2 e_i^2 \phi_{ii} + \frac{1}{2} \sum_{i=1}^3 |A_i|^2 \phi_0 + \sum_{1 \leq i < j \leq 3} A_i \overline{A_j} e_i \overline{e_j} \phi_{ij} \right) + c.c.. \quad (18)$$

Notice that ϕ_{ii} and ϕ_{ij} are independent of i and j . Using this notation, one can see that ϕ_{ii} and ϕ_{ij} correspond to A_i^2 and $A_i \overline{A_j}$, respectively. Substituting (18) into (16) and sorting with respect to e_m^n , yields

$$\begin{aligned} A_i^2 e_i^2 : & \quad B(\Phi, \Phi) + L(2k)\phi_{ii} = 0 & \Rightarrow & \quad \phi_{ii} = -L(2k)^{-1} B(\Phi, \Phi) \\ |A_i|^2 : & \quad 2B(\Phi, \overline{\Phi}) + L(0)\phi_0 = 0 & \Rightarrow & \quad \phi_0 = -2L(0)^{-1} B(\Phi, \overline{\Phi}) \\ A_i \overline{A_j} e_i \overline{e_j} : & \quad 2B(\Phi, \overline{\Phi}) + L(\sqrt{3}k)\phi_{ij} = 0 & \Rightarrow & \quad \phi_{ij} = -2L(\sqrt{3}k)^{-1} B(\Phi, \overline{\Phi}) \end{aligned}$$

To remove terms of order e_i from the residual, we extend the ansatz (18) to $\tilde{w} = w + \sum_{i=1}^3 \phi_{3i} e_i$. Substituting \tilde{w} into (16) and sorting with respect to e_1, e_2, e_3 , yields

$$\begin{aligned} e_1 : \quad & \hat{L}(k)\phi_{31} = -\partial_T A_1 + d_1 A_1 + d_2 \overline{A_2 A_3} + d_3 A_1 |A_1|^2 + d_4 A_1 (|A_2|^2 + |A_3|^2) + R_1, \\ e_2 : \quad & \hat{L}(k)\phi_{32} = -\partial_T A_2 + d_1 A_2 + d_2 \overline{A_1 A_3} + d_3 A_2 |A_2|^2 + d_4 A_2 (|A_1|^2 + |A_3|^2) + R_2, \\ e_3 : \quad & \hat{L}(k)\phi_{33} = -\partial_T A_3 + d_1 A_3 + d_2 \overline{A_1 A_2} + d_3 A_3 |A_3|^2 + d_4 A_3 (|A_1|^2 + |A_2|^2) + R_3, \end{aligned} \quad (19)$$

$$\begin{aligned} \text{with} \quad & d_1 = \mu(k)\Phi, \\ & d_2 = 2B(\overline{\Phi}, \overline{\Phi}), \\ & d_3 = 3C(\Phi, \Phi, \overline{\Phi}) + 2B(\overline{\Phi}, \phi_{ii}) + 2B(\Phi, \phi_0), \\ & d_4 = 6C(\Phi, \Phi, \Phi) + 2B(\Phi, \phi_{ij}) + 2B(\Phi, \phi_0). \end{aligned}$$

The summands R_1, R_2, R_3 represent all higher order terms, e.g., $A_1 |A_2|^4$ is a term of R_1 . By the Fredholm alternative there exists a solution for (19), iff the r.h.s. is an element of $\ker(\hat{L}(k)^H)^\perp$. Let Φ^* be the adjoint eigenvector of $\hat{L}(k)$ to the eigenvalue $\mu(k)$ evaluated in σ_k , i.e., $\hat{L}(k)^H \Phi^* = \overline{\mu(k)} \Phi^*$, and let Φ^* be normalized such that $\langle \Phi, \Phi^* \rangle = 1$. Multiplying (19) with Φ^* and setting $R_1 = R_2 = R_3 = 0$, yields

$$\begin{aligned} \partial_T A_1 &= f_1(A_1, A_2, A_3) := c_1 A_1 + c_2 \overline{A_2 A_3} + c_3 A_1 |A_1|^2 + c_4 A_1 (|A_2|^2 + |A_3|^2), \\ \partial_T A_2 &= f_2(A_1, A_2, A_3) := c_1 A_2 + c_2 \overline{A_1 A_3} + c_3 A_2 |A_2|^2 + c_4 A_2 (|A_1|^2 + |A_3|^2), \\ \partial_T A_3 &= f_3(A_1, A_2, A_3) := c_1 A_3 + c_2 \overline{A_1 A_2} + c_3 A_3 |A_3|^2 + c_4 A_3 (|A_1|^2 + |A_2|^2), \end{aligned} \quad (20)$$

where $c_i = \langle d_i, \Phi^* \rangle$. The classical Landau reduction evaluates $c_2, c_3, c_4, \Phi, \phi_{ii}, \phi_{ij}, \phi_0$ in σ_c and c_1 in σ . One can see in [22] that evaluating them all in σ can give better approximations. However, in the following we use the Landau reduction to predict the existence and bifurcation directions of stationary states which branch from homogeneous solutions. To approximate solutions and follow their branches we use `pde2path`.

This method works also and yields the same system (20) and Landau coefficients, if we use phase shifted space coordinates in the ansatz, i.e., using $(x + \psi, y + \psi)$ with $\psi \in (0, 2\pi)$ instead of (x, y) .

4 1D Patterns

First we consider solutions over one dimensional domains. Here the modes e_2 and e_3 do not exist. Hence, the system (20) reduces to

$$\partial_t A = c_1 A + c_3 |A|^2 A. \quad (21)$$

Stationary amplitudes solve

$$c_1 A + c_3 |A|^2 A = 0. \quad (22)$$

Clearly $A = 0$ solves (22). Setting this solution into the ansatz (18), yields the homogeneous solution. More interesting are the second type of solutions which we obtain from (22). They fulfill

$$|A| = \sqrt{-\frac{\mu(k)}{c_3}} \quad (23)$$

and generate periodic solutions by substituting $(A_1, A_2, A_3) = (A, 0, 0)$ into (18). This type of solutions exists also in 2D and we call these solutions stripes because of their 2D-density plot. When we use numerical methods to determine the stripes in the following, we use Neumann boundary conditions. Stripes which fulfill Neumann boundary conditions over a domain $(-l\pi/k, l\pi/k)$ with $l \in \mathbb{N}$ correspond to the amplitudes

$$S_\pm = \pm \sqrt{-\frac{\mu(k)}{c_3}}.$$

If the bacteria density u has its maximum (minimum) in $x = 0$ for such a stripe solution, we call it hot (cold) stripes. Notice that we do not have automatically hot and cold stripes for S_+ and S_- , respectively. All other amplitudes which fulfill (23) generate space shifts of the hot resp. cold stripes.

Let σ_k be a bioirrigation value and $k \in \mathbb{R}^+$ a wavenumber such that the curve of eigenvalues μ for σ_k has a single zero in k . Let σ_s and σ_l be two bioirrigation values, which are infinitesimally smaller and larger than σ_k , respectively. It holds that the curve of eigenvalues μ is positive in k for σ_s or σ_l , while it is negative for the other. The stripes can only exist, where (23) is fulfilled such that the algebraic sign of c_3 evaluated in σ_k tells us in which direction the stripes bifurcate.

4.1 Changing wavelength

We start a global analysis of 1D patterns in (2) for $\gamma = 0.3$. From our analysis above we already know that we still have one homogeneous solution for all $\sigma \in (0, 0.25)$ with an unstable range bounded by Turing bifurcation points. Furthermore, we know that there are two Turing endpoints in this unstable range. We use our data set of Fig.3 to find out that the right and left Turing bifurcation points are given by $\sigma_c^r \approx 0.11$ and $\sigma_c^l \approx 0.025$ with corresponding critical wave numbers $k_c^r \approx 0.187$ and $k_c^l \approx 0.067$, respectively. The curve of eigenvalues μ_{\pm} (see (12)) has a zero in k , when $\det L(k) = 0$. This is the case for

$$k_{\pm} = \sqrt{\frac{dg_u + h_v}{2d} \pm \sqrt{\left(\frac{dg_u + h_v}{2d}\right)^2 + \frac{g_v h_u - g_u h_v}{d}}}.$$

Clearly in the Turing unstable range it holds $k_{\pm} \in \mathbb{R}$. We proved that this is also the case between the Turing endpoints.

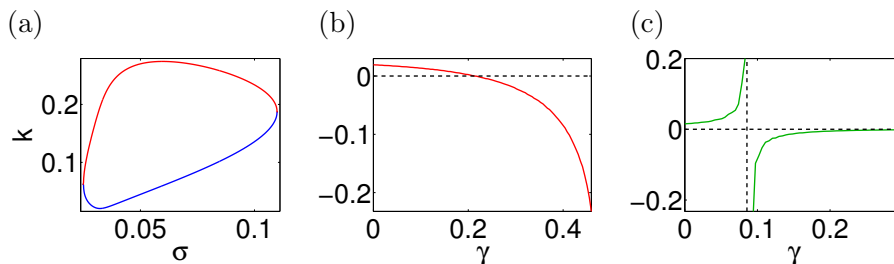


Figure 6: (a) The blue and red curves represents k_- and k_+ for $\gamma = 0.3$. (b) c_3 and $c_f = c_2^2/(4(c_3 + 2c_4)^2)$ evaluated in σ_c as function of γ are shown in (b) and (c) and used to predict the strength of the subcriticality of stripes and hexagons, respectively. Hexagon patterns will be introduced in Section 5.

The Landau formalism above predicts that periodic solutions of the type

$$(u, v) = (u^*, v^*) + 2A \cos(kx)\Phi + \text{h.o.t.} \quad (24)$$

bifurcate from (u^*, v^*) at σ_c^r with $k = k_c^r$, if we consider the problem over the 1D domain $\Omega^r = (-4\pi/k_c^r, 4\pi/k_c^r)$. We are able to prove analytically that there are bioirrigations $\sigma_{35}, \sigma_{45}, \sigma_3$ with $\sigma_c^r > \sigma_{35} > \sigma_{45} > \sigma_3$, where branches $R35, R45$, and $R3$ of periodic solutions of the type (24) bifurcate with $k = 3.5k_c^r/4, 4.5k_c^r/4$, and $3k_c^r/4$, respectively. Let $s \in \{\sigma_c^r, \sigma_{35}, \sigma_{45}, \sigma_3\}$ and κ be the corresponding wavenumber. In Fig.6(a) we see that a bioirrigation value $s_2 \neq s$ in the unstable range exists for which the eigenvalue curve μ_{\pm} has a real zero in κ such that a stripe solution with wavenumber κ also branches in s_2 . Following the branches with `pde2path` [23] which bifurcate in s , we see that they terminate in s_2 (see Fig.7).

One may conjecture that stripe branches which correspond to the same wavenumber are connected, but this is not always the case. We also computed the branch L4 which bifurcates in σ_c^l with the critical wavenumber k_c^l over the domain $\Omega^l = (-4\pi/k_c^l, 4\pi/k_c^l)$. In Fig.6(a) we see that there is $\sigma \neq \sigma_c^l$, where stripe solutions of the wavelength k_c^l bifurcate. We call the corresponding solution branch L4*. In Fig.8 we see that L4 and L4* are not connected, but they connect to bifurcations on L8 and L16, which are stripe solutions of 4 and 16 periods, respectively. One might guess that this depends on the Turing endpoints. However, we also compute the branches for $\gamma = 0.4$ (not shown). Here we have no Turing endpoints, but the same effects.

(a) global 1D bifurcation diagram

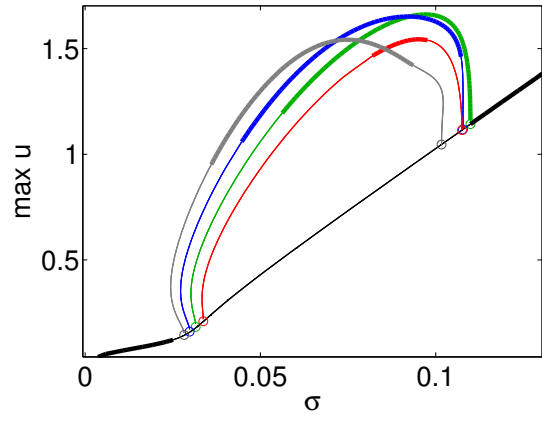
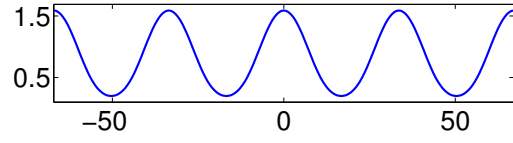
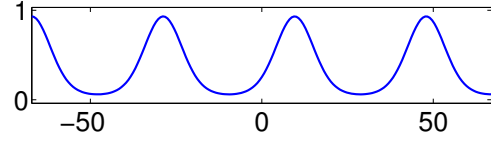
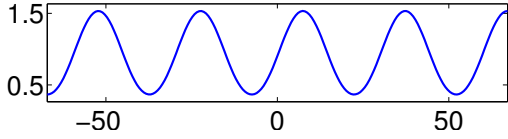
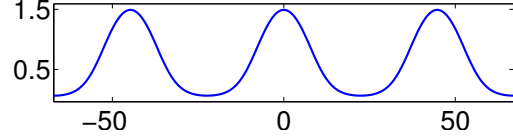
(b) u of R4 for $\sigma = 0.08$ (c) u of R35 for $\sigma = 0.09$ (d) u of R45 for $\sigma = 0.04$ (e) u of R3 for $\sigma = 0.06$ 

Figure 7: All plots are for $\gamma = 0.3$ and the domain $\Omega^r = (-4\pi/k_c^r, 4\pi/k_c^r)$. (a) From the first, second, third, and fourth bifurcation point (counting from the right side) of the homogeneous branch (black) bifurcate branches of periodic solutions with 4 (green), 3.5 (blue), 4.5 (red), and 3 (gray) periods, which we call R4, R35, R45, and R4, respectively. Example solutions of R4, R35, R45, and R4 are shown in (b), (c), (d), and (e), respectively. All these example solutions are stable. Here and for all coming calculations for which we used `pde2path` we always use Neumann boundary conditions, and thick and thin parts of the branches represent stable and unstable solutions, respectively.

(a)

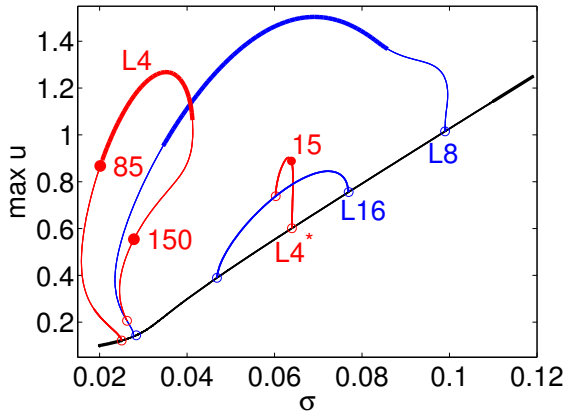
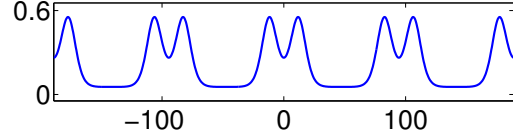
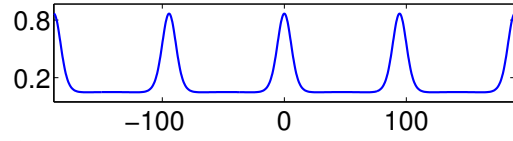
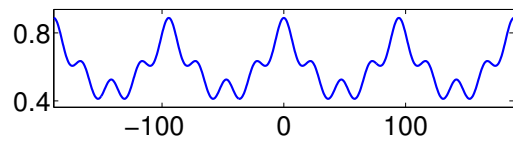
(b) u at points 85 and 150 of L4(c) u at point 15 of L4*

Figure 8: All plots are for $\gamma = 0.3$ and the domain $\Omega^l = (-4\pi/k_c^l, 4\pi/k_c^l)$. (a) On L8 and L16 we have always solutions of 8 and 16 periods, respectively. Both branches bifurcate and terminate on the homogeneous solution branch (black). L4 and L4* bifurcate from the homogeneous solution branch as periodic solutions with 4 periods and terminate on L8 and L16, respectively. Example solutions of L4 and L4* are shown in (b), (c), (d), and (e), respectively.

4.2 Localized patterns and snaking

The Landau coefficient c_3 evaluated in σ_c are positive for $\gamma \in (0, 0.209)$ (see Fig.6(b)) and thus stripes bifurcate subcritically for these active stimulations. We calculate the branch \mathbf{s} of hot-stripes (u_s, v_s) by using `pde2path` for $\gamma \approx 0.004$ over the domain $\Omega = (-24\pi/k_c, 24\pi/k_c)$ with $k_c = 0.212$. \mathbf{s} bifurcates subcritically from the homogeneous solution $(u^*, v^*) = (u_1, v_1)$ at $\sigma_c \approx 0.196$, as predicted by the Turing and Landau analysis above. A fold occurs at $\sigma \approx 0.1985$ and the stripes become stable such that there is a bistable range between (u^*, v^*) and (u_s, v_s) .

There are 10 bifurcation points on \mathbf{s} on the way from its bifurcation to the fold. The first and 10th, second and 9th, third and 8th, 4th and 7th, 5th and 6th are connected pairwise by branches of stationary fronts between stripes and homogeneous states, which we call 11, 12, 13,

14, and 15, respectively (see Fig.9, 10, and 11).

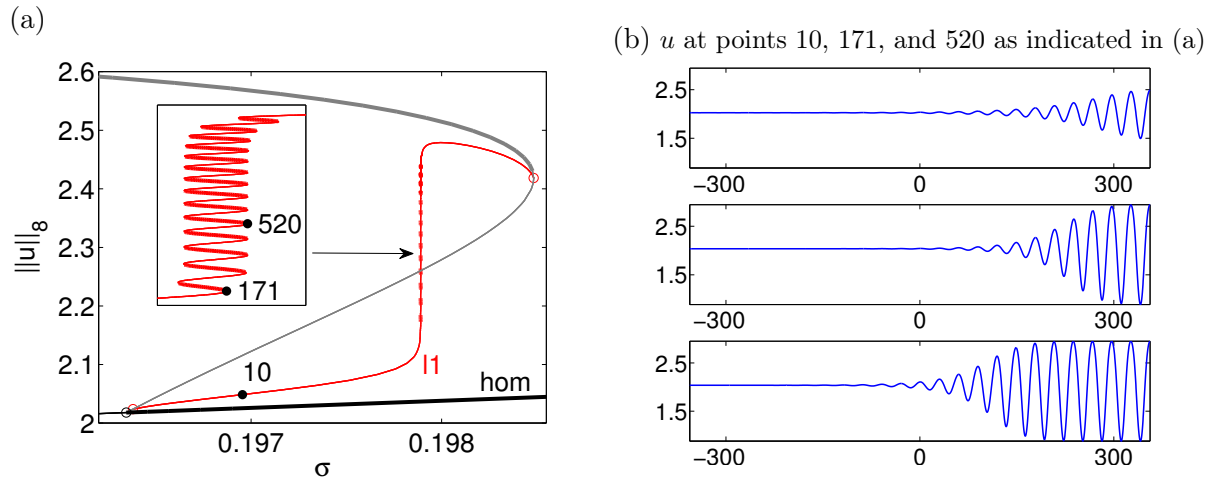


Figure 9: (a) Bifurcation diagram for 1D patterns over the domain $\Omega = (-24\pi/k_c, 24\pi/k_c)$ for $\gamma = 0.004$ including the homogeneous solution (black), hot stripes (gray), and the branch of stationary heteroclinics 11 (red) which bifurcates from the first bifurcation point of the hot stripes. The right and left horizontal boundaries of the zooming-in of the snake are 0.197889 and 0.197891. (b) Plots of u for solutions which are labeled in (a). The other branches which bifurcate from the hot stripe branch are illustrated Fig.10 and Fig.11

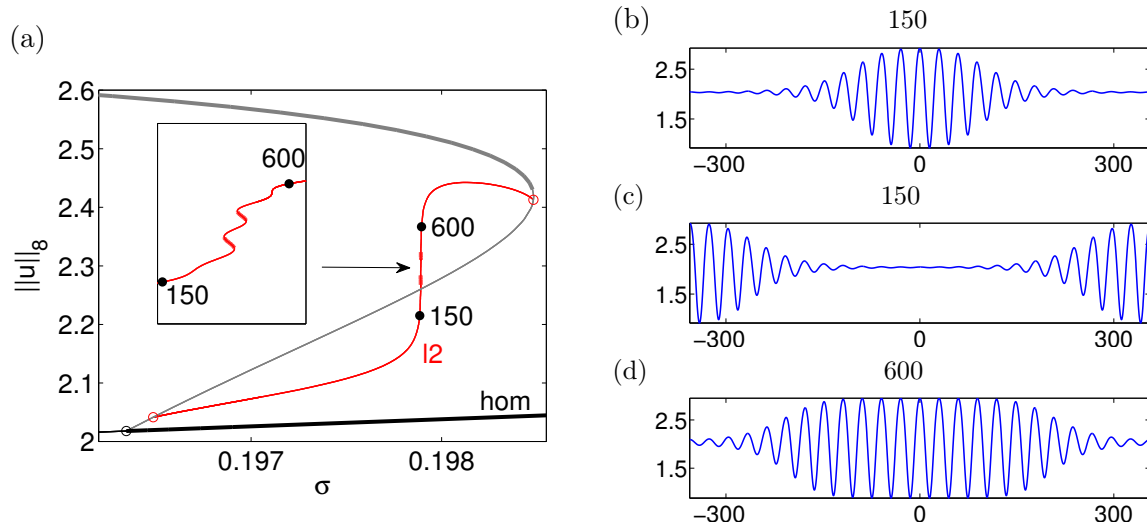


Figure 10: (a) Bifurcation diagram for the branch 12 of homoclinics between the homogeneous and stripe solution which bifurcates from the second bifurcation point of the hot stripes. Plots of u for solutions of 12 at points 150 and 600 are shown in (b) and (d), respectively. (c) u at point 150 by using the negative tangent of the one we used to bifurcate on 12.

Solutions of 11 are oscillations of the type

$$u = u^* + A \cos(k_c x) + \text{h.o.t.}, \quad v = v^* + B \cos(k_c x) + \text{h.o.t.} \quad (25)$$

with monotonously spatially growing amplitudes A and B on Ω . For simplicity we still describe the behavior of u in the following.

Clearly the amplitude A_s for u_s is constant. By following 11 from the first bifurcation point on \mathbf{s} to the first fold, which lies near the 171st solution, u transforms to a front between u^* and u_s . After this 11 "snakes" back and forth by changing its stability. Along the snake the front moves from the right to the left, and the front position shifts by $\pi/(2k_c)$ between two successive folds. Beyond the last fold A starts to grow at the left boundary and 11 returns to \mathbf{s} .

For every solution of 11 also exists a reflection. We call the corresponding branch 11'. Clearly the illustration of 11' is congruent with 11 and both branches together generate a loop from one bifurcation point to the other and back again.

Splitting the domain Ω into $\Omega_l = (-24\pi/k_c, 0)$ and $\Omega_r = (0, 24\pi/k_c)$, we can describe solutions on 12 as two heteroclinics on Ω_l and Ω_r , where the one on Ω_r is a reflection of the one

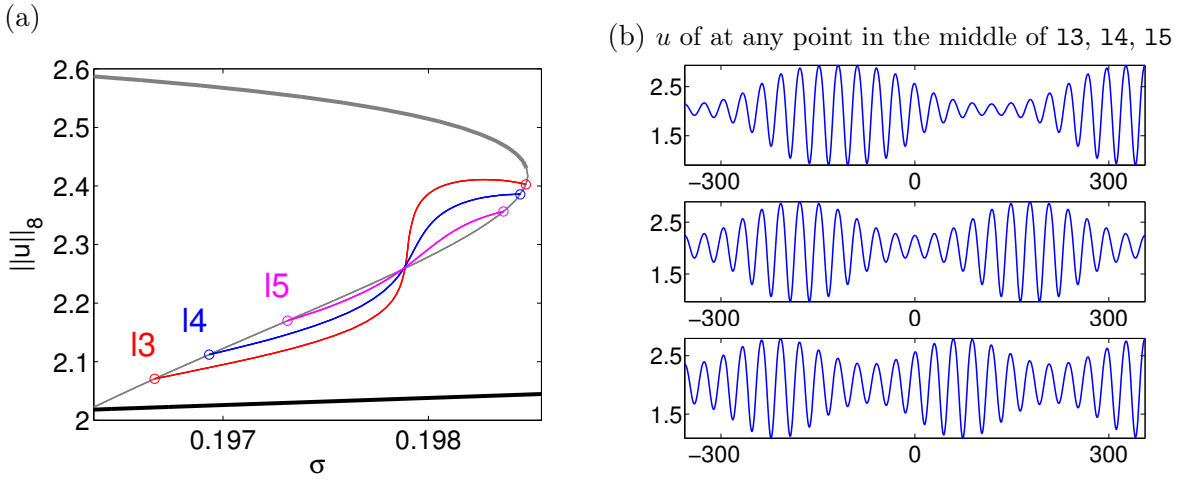


Figure 11: (a) Bifurcation diagram for the branches of multi localized stripes 13, 14, and 15 which bifurcates from the third, fourth, and fifth bifurcation point of the hot stripes, respectively. (b) u on 13, 14, and 15.

on Ω_l . Here the snake is shorter with fewer wiggles, because the lengths of the domains Ω_l and Ω_r are shorter than the length of Ω such that the fronts move faster to the boundaries of Ω_l and Ω_r . We can split the domain Ω into 3, 4, and 5 parts and use heteroclinics like above to describe solutions of 13, 14, and 15, respectively. Here the branches do not show any snaking behavior, because the partitions of Ω are too small. The same branches for connections between cold stripes and the homogeneous solutions can be found on the cold-stripe branch.

Additional localized stripes of the form

$$u = u^* + A \sin(k_c x) + \text{h.o.t.} \quad (26)$$

exist for periodic boundary condition. The illustrations of the corresponding branches d1, d2, d3, d4, and d5 (not shown) are not congruent with 11, 12, 13, 14, and 15, respectively. The folds of 11 and d1, ..., 15 and d5 are connected pairwise by branches, which are called rungs. Using Dirichlet or Neumann boundary conditions, we can only find solutions of the form (26) or (25), respectively. Currently periodic boundary conditions are not implemented in `pde2path` but will be added.

For more details on localized patterns and snaking over bounded dimensional domains see [4, 11, 17, 16]. Seminal results for localized patterns over unbounded domains can be found in [6, 7, 3]. For a detailed analysis by using the Ginzburg-Landau formalism and beyond all order asymptotics see [10, 13].

5 2D Patterns

The stripe patterns also exist over two dimensional domains. Here we present additionally some genuine 2D patterns, which can be analyzed via the Landau system (20). Setting $A_1 = A_2 = A_3 =: A$, the system (20) reduces to

$$\partial_t A = c_1 A + c_2 \bar{A}^2 + (c_3 + 2c_4) A |A|^2.$$

Stationary amplitudes fulfill

$$c_1 A + c_2 \bar{A}^2 + (c_3 + 2c_4) A |A|^2 = 0.$$

Two types of non homogeneous solutions can be found from this equation. These are hexagon and triangle patterns with $A \in \mathbb{R}$ and $A \in \mathbb{C} \setminus \mathbb{R}$, respectively. The hexagon amplitudes are given by

$$A = H_{\pm} := -\frac{c_2}{2(c_3 + 2c_4)} \pm \sqrt{\frac{c_2^2}{4(c_3 + 2c_4)^2} - \frac{\mu(k_c)}{c_3 + 2c_4}}. \quad (27)$$

The triangle amplitudes are given by $a_1 + a_2i$ solving

$$-(c_3 + 2c_4)a_1^3 - c_2(c_3 + 2c_4 + 1)a_1^2 + 2\left(c_1 - \frac{c_2^2}{c_3 + 2c_4}\right)a_1 + \frac{c_1c_2}{c_3 + 2c_4} = 0$$

$$\text{with } a_2 = \sqrt{\frac{c_1 - 2c_2a_1 + (c_3 + 2c_4)a_1^2}{c_3 + 2c_4}}.$$

Setting $(A_1, A_2, A_3) = (A, B, B)$ into (20) one can find mixed mode solutions. We classify them into bean and rectangle patterns, which fulfill $|A| > |B|$ and $|A| < |B|$, respectively.

Fig.12 shows some bifurcation diagrams over a small 2D domain. In Fig.12(a) we see that when the hot stripes lose their stability, a branch of hot beans bifurcates subcritically, which terminates in a bifurcation on the hot hexagon branch in the point where these become stable. An analog scenario occurs in the bistable range between cold hexagons and cold stripes (see Fig.12(b)).

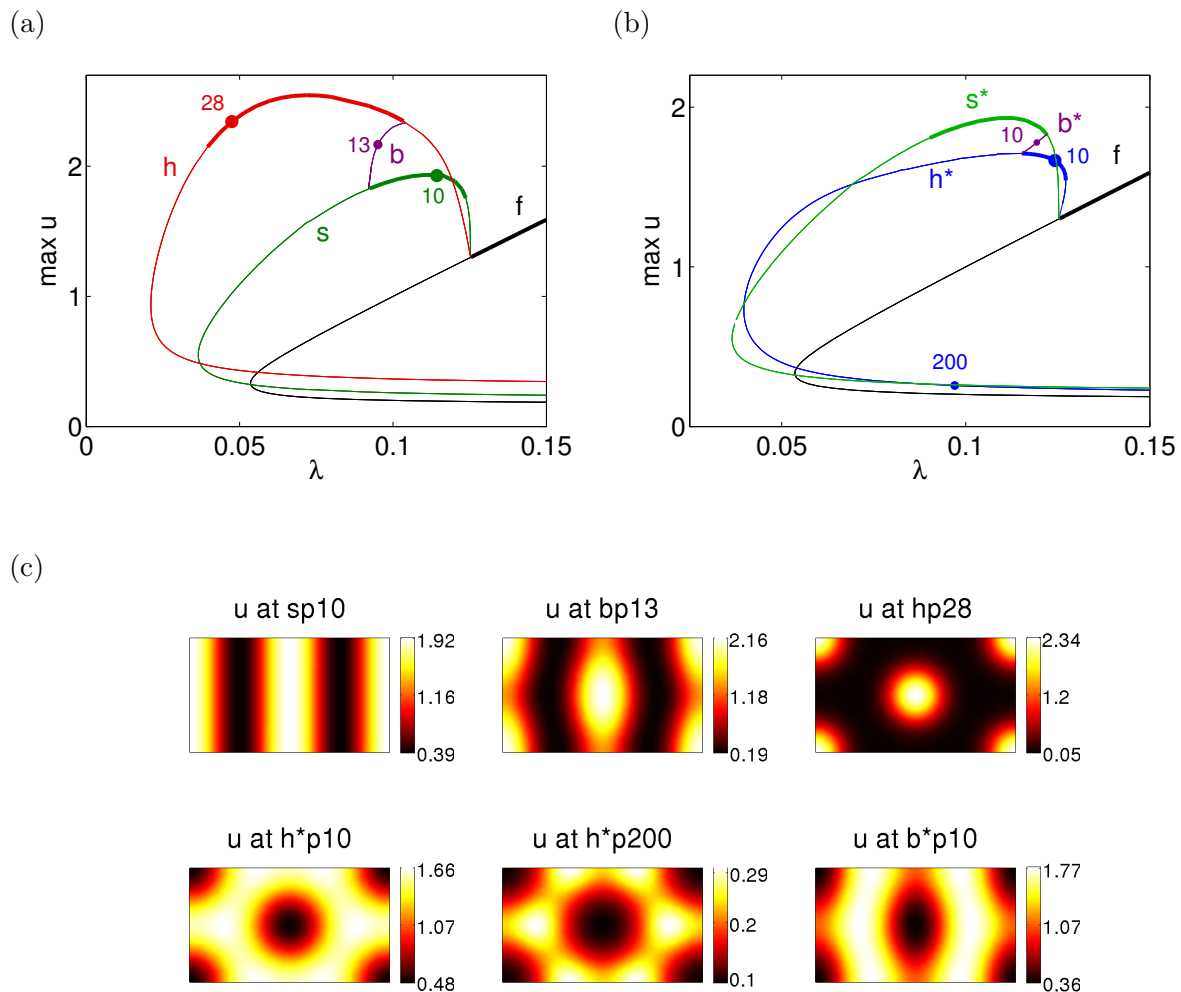


Figure 12: (a), (b) Bifurcation diagrams for $\gamma = 0.25$ over the domain $(-l_x, l_x) \times (-l_y, l_y)$, where $l_x = 2\pi/kc$, $l_y = 2\pi/(\sqrt{3}k_c)$, and $k_c \approx 0.19$. f represents the homogeneous solution. The red, green, and violet lines in (a) are branches of hot hexagons h , hot stripes s , and hot beans b , respectively. The blue, green, and violet lines in (b) represents branches of cold hexagons h^* , cold stripes s^* , and cold beans b^* , respectively. (c) Density plots for solutions which are labeled in (a) and (b). Here and in the following means an abbreviation of a plot's title like 'u at sp10' that this is u for the 10th solution which is labeled on the branch s .

Over this small domain the hot-bean branch has 4 bifurcation points (not indicated). By increasing the horizontal direction by a factor of 4, the number of bifurcation points on the hot-bean branch also increases by a factor of 4 (see Fig.13) with bifurcations of stationary connections between stripes and hot hexagons. Here everything is analog to the 1D case described above.

The bifurcation points are connected in the same way. From the first one bifurcates a snaking branch of solutions, which we see again as front between hot stripes and hot hexagons. From the second bifurcates a branch of two interfaced heteroclinics, and this holds analogously for the other bifurcating solutions of the hot-bean branch.

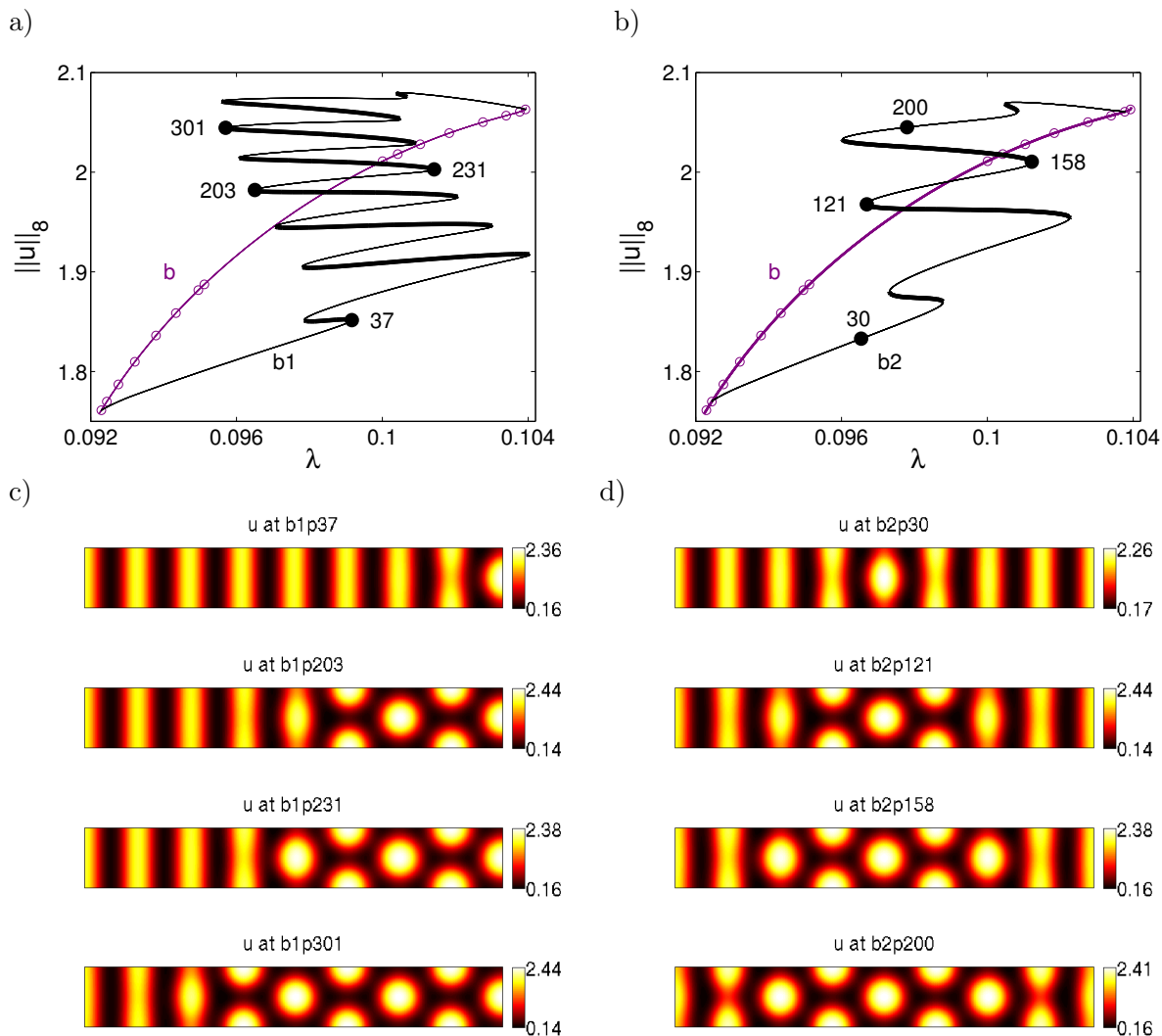


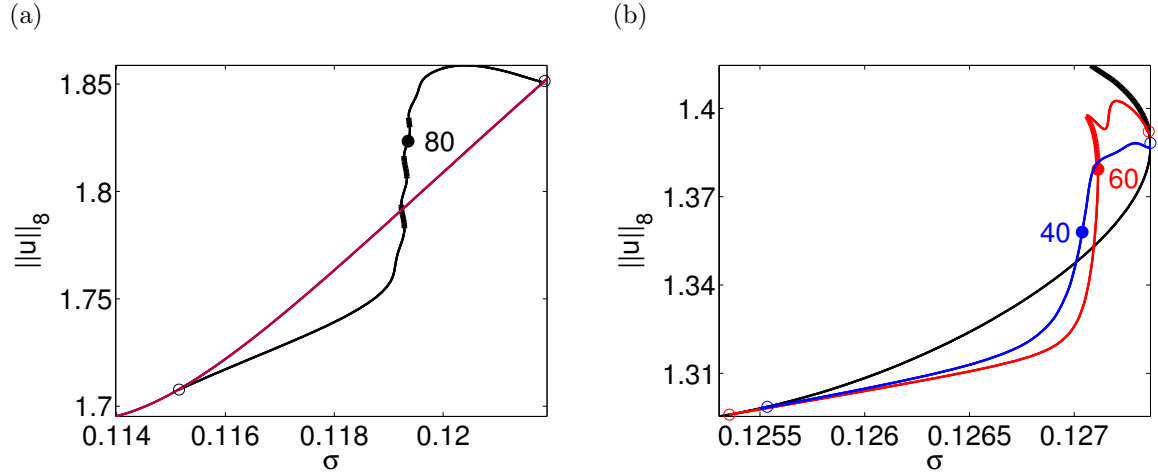
Figure 13: Density plots and bifurcation diagrams of solutions of (2) for $\gamma = 0.25$ over the domain $(-l_x, l_x) \times [-l_y, l_y]$, where $l_x = 8\pi/kc$ and $l_y = 2\pi/(\sqrt{3}kc)$. a) Bifurcation diagram of fronts between hot spots and stripes. b) Bifurcation diagram of localized hot spots on a striped background. c) and d) density plots of solutions labeled in a) and b), respectively.

In contrast to the 1D case the snake does not snake around a vertical line but in a slanted manner. This is a finite size effect; cf. [5, 4, 16, 12]. Such localized patterns can also be found on cold bean branches (see Fig.14(a)). It can be seen in (27) that one hexagon type (hot or cold) bifurcates sub- and the other supercritically such that there is a bistable range between the homogeneous and hexagon solution.

We use a triangular domain to calculate branches of localized hexagons on homogeneous backgrounds for $\gamma = 0.25$. The solutions which bifurcate from the first and second bifurcation points of the cold hexagon branch are a single localized patch and multi localized patches of hexagons, respectively. Here only the single patch exhibits a snaking behavior with only one wiggle. By increasing the domain size, the number of wiggles should increase for both.

Under the assumption that the Landau coefficients c_2, c_3, c_4 change much slower than c_1 when varying σ away from σ_c , we can see in (27) that the subcriticality increases, if $c_f := c_2^2/(4(c_3 + 2c_4)^2)$ increases. c_f evaluated in σ_c as function of γ is shown in Fig.6(c). For $\gamma \approx 0.08$ it holds $c_3 + 2c_4 = 0$ such that we assume that we can increase the strength of subcriticality and with that the front's steepness and the width of snaking ranges by choosing a γ -value closer to 0.08. A similar prediction of the strength of subcriticality and width of the snaking branch for

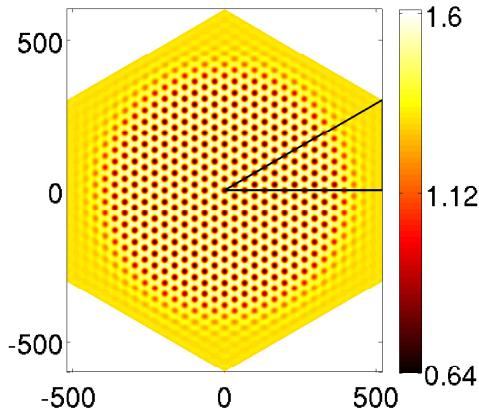
bean branches on a Landau level can be found in [22].



(c) 80th solution of the black branch in Fig.14(a)



(d) 60th solution of the red branch in Fig.14(b)



(e) 40th solution of the blue branch in Fig.14(b)

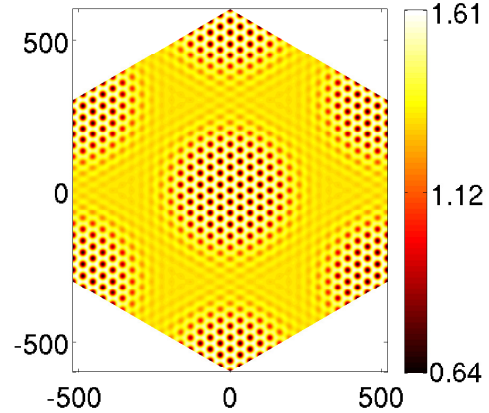
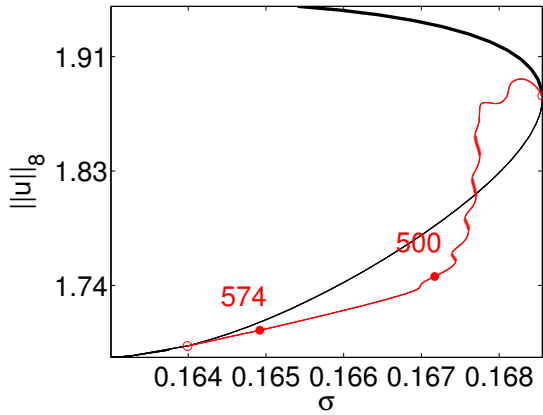


Figure 14: All plots are for $\gamma = 0.25$. (a) Bifurcation diagram over the domain $(-l_x, l_x) \times (-l_y, l_y)$, where $l_x = 16\pi/k_c$, $l_y = 2\pi/(\sqrt{3}k_c)$, and $k_c \approx 0.19$. The violet and black lines represent the branches of cold beans and localized cold hexagons on a striped background. (b) Bifurcation diagram over a triangular domain, which is given by the vertices $(0, 0)$, $(32\pi/k_c, 0)$, and $(32\pi/k_c, 32\pi/(\sqrt{3}k_c))$. The black line represents the branch of cold hexagons, while the red and blue lines are the branches which bifurcate at the first and second bifurcation points after the fold of the cold hexagons, respectively. (c), (d), (e) Density plots of the solutions which are labeled in (a) and (b). For (d) and (e) we reflected and rotated the triangular domain to get a hexagonal domain.

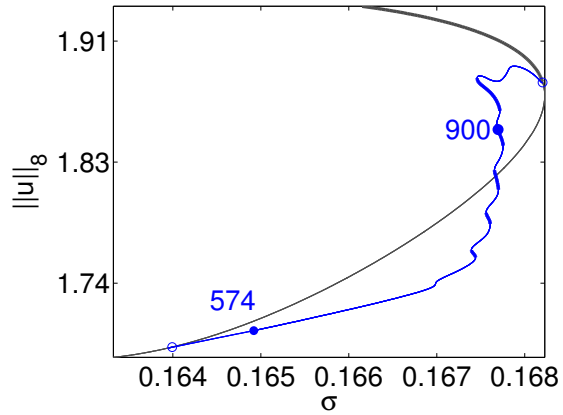
In Fig.15(a) we see that the branch of single patches already shows a snaking behavior with more than one wiggle for $\gamma = 0.12$ over a domain which is smaller than the domain which we used for $\gamma = 0.25$. The front of the 574th solution becomes so steep that it looks like one single spot. From this point bifurcates a branch of a single hexagon patch which is rotated by $\pi/6$. Between the 574th and 900th solutions the branches in Fig.15(a) and (b) seem to be congruent. Behind the 900th solution the boundary affects the rotated patches and the branch moves to a branch of stretched hexagons.

(a) Bifurcation diagram for regular hexagons

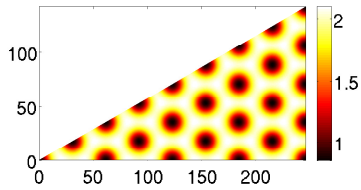


(c) Fold of the black branch in (a)

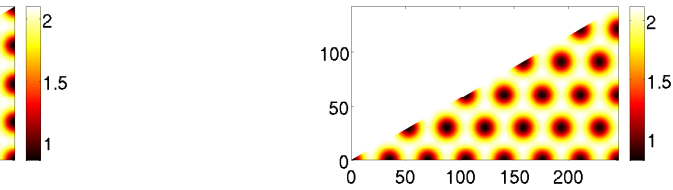
(b) Bifurcation diagram for stretched hexagons



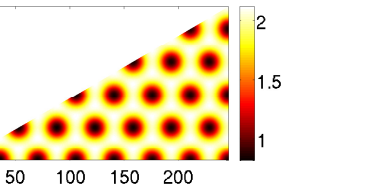
(d) Fold of the gray branch in (b)



(e) 574 in (a) and (b)



(f) 500 in (a)



(g) 900 in (b)

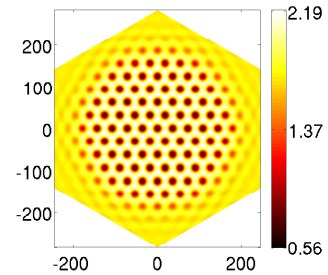
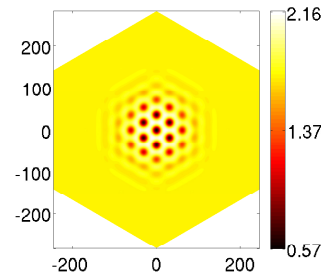
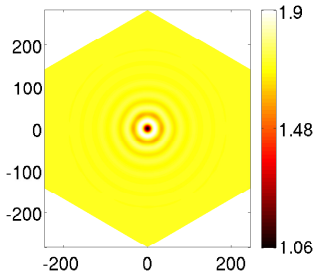


Figure 15: All plots are for $\gamma = 0.12$. (a) Bifurcation diagram over a triangular domain, which is given by the vertexes $(0, 0)$, $(16\pi/k_c, 0)$, and $(16\pi/k_c, 16\pi/(\sqrt{3}k_c))$. The black and gray lines in (a) and (b) represent the branches of regular and stretched cold hexagons, while the red and blue lines are branches which bifurcate from the first bifurcation point after the fold of the cold hexagons, respectively. (c), (d) Density plots of regular and stretched hexagons on the triangular domain. (e), (f), (g) Density plot of the solution which is labeled in (a) and (b). Here we reflected and rotated the triangular domain to get a hexagonal domain.

6 Discussion

We investigated the system (2) for homogeneous bioirrigations σ . First we gave analytical formulas for the homogeneous states and determined stable, unstable, and Turing-unstable regions of the σ - γ -plane. We classified bifurcation points, which lie at the boundaries of the Turing-unstable range into Turing endpoints and Turing bifurcation points. At the first one occurs Hopf bifurcations, which we did not study.

We turned our main attention to localized patterns and used `pde2path` to compute branches of localized stripes, localized single, and multi hexagon patches on homogeneous backgrounds. All these branches have a snaking behavior. We used the Landau reduction to understand the structure of the patterns which bifurcate from the Turing bifurcation points, to see for which γ -values bifurcate stripes resp. hexagons subcritically, and to predict the strength of subcriticality and snaking behavior. We also computed branches of localized hexagons on striped backgrounds. A similar analysis for such branches can be found in [22] for an other reaction-diffusion system.

There is already a large number of investigations of localized stripes and snaking branches over 1D domains. See for instance [4, 11, 17, 16] for studies over bounded domains, [6, 7, 3] for results over unbounded domains, and [10, 13] for a detailed analysis by using the Ginzburg-Landau

formalism and beyond all order asymptotics. There are not so many investigations of localized states over 2D domains. It is already pointed out in [21] on a Ginzburg-Landau level that all the localized 2D structures mentioned above should exist in reaction-diffusion systems. Some localized patches of hexagons and stationary fronts between hexagons and stripes are found for the quadratic-cubic Swift-Hohenberg equation in [15] via time integrations. Branches of localized single hexagon patches on a homogeneous background for this equation are first studied numerically and analytically in [19]. In the present paper we show the first numerical calculation of a branch of multi hexagon patches. Branches of localized hexagons on striped backgrounds are first investigated in [22]. We restrict ourselves to planar interfaces between hexagons and stripes. Localized hexagon patches on striped backgrounds are shown in the outlook of [22]. Here the hexagons are stretched and the authors were not able to find such patches for regular hexagons and neither the corresponding vertical fronts, and it is still an open problem whether patches of regular hexagons on striped backgrounds exist.

We also developed numerically some 1D global bifurcation diagrams. We found two stripe branches of the same wavelength, which are not connected, but connect to branches of a different wavelength (see Fig.8), and branches of the same wavelength, which are connected (see Fig.7). Understanding these behaviors is an interesting study for a further work.

From these studies we learn that a layering of two patterns is not necessarily an effect of space dependent bifurcation parameters but can occur for homogeneous bioirrigations. Thus we postpone a bifurcation analysis of patterns for depth dependent bioirrigations. Furthermore, we postpone the following issues. For $\gamma = 0.25$ exist rectangle patterns, when the stripes are stable and the hexagons are unstable. Their branch connects the branches of cold and hot hexagons. We computed branches over bounded domains of the form $(-2l\pi/k_c, 2l\pi/k_c) \times (-2\pi/(\sqrt{3}k_c), 2\pi/(\sqrt{3}k_c))$ and found stable rectangles, which bifurcate from the hot and cold hexagons and become unstable in the middle. Increasing l , increases the unstable part. Thus we suspect that the rectangle branch is always unstable over unbounded domains. However, over bounded domains of the form like above there is a bistable range between rectangles and stripes. When the rectangles lose their stability, a snaking branch (with stable parts) bifurcates for which the solutions look like fronts between rectangles and stripes, but we can not find where the branch terminates.

We did not find bistable ranges of hot and cold hexagons, which exist for instance for the Rayleigh-Bénard convection (see Fig.10 of [14]). In this bistable range a branch of triangle patterns exists which connects both hexagon branches. This is analogously to bean branches and we suspect that branches of fronts between cold and hot hexagons bifurcate from this triangle branch. In this paper we did not study any triangle patterns, because they fulfill periodic but not Neumann boundary conditions. The current version of `pde2path` does not handle periodic boundary conditions, but an add-on is already under construction.

It can already be seen by considering the Jacobians of (20) and (21) that the stripes which correspond to S_+ bifurcate stable in 1D and unstable in 2D for negative c_3 and positive c_2 and c_4 . We expect that some of the stable solutions presented here, trivially extended in z direction, are not stable over 3D domains. Since the sediment is 3D, an investigation of the bacteria-nutrient model (1) over 3D domains is appropriate. A 3D version of `pde2path` is under construction, and preliminary numerical studies of Turing bifurcations in 3D show that the many more different patterns make an analysis much more difficult, as expected. See also [18, 1] for experimental and numerical investigations of 3D patterns. Classifications of 3D Turing patterns by symmetries and Landau reductions can be found in [8, 9].

References

- [1] T. Bánsági, V. K. Vanag, and Irving R Epstein. Tomography of reaction-diffusion microemulsions reveals three-dimensional turing patterns. *Science*, 331(6022):1309–1312, 2011.
- [2] M. Baurmann, W. Ebenhöf, and U. Feudel. Turing instabilities and pattern formation in a benthic nutrient-microorganism system. *Math. Biosci. Eng.*, 1(1):111–130, 2004.

- [3] M. Beck, J. Knobloch, D.J.B. Lloyd, B. Sandstede, and T. Wagenknecht. Snakes, ladders, and isolas of localized patterns. *SIAM J. Math. Anal.*, 41(3):936–972, 2009.
- [4] A. Bergeom, J. Burke, E. Knobloch, and I. Mercader. Eckhaus instability and homoclinic snaking. *Phys.Rev.E*, 78:025201, 2008.
- [5] U. Bortolozzo, M. G. Clerc, and S. Residori. Local theory of the slanted homoclinic snaking bifurcation diagram. *Phys. Rev. E*, 78:036214, Sep 2008.
- [6] J. Burke and E. Knobloch. Localized states in the generalized Swift-Hohenberg equation. *Phys. Rev. E*, 73:056211, May 2006.
- [7] J. Burke and E. Knobloch. Homoclinic snaking: Structure and stability. *Chaos*, 17(3):037102, 15 p., 2007.
- [8] T. K. Callahan and E. Knobloch. Symmetry-breaking bifurcations on cubic lattices. *Nonlinearity*, 10(5):1179, 1997.
- [9] T. K. Callahan and E. Knobloch. Pattern formation in three-dimensional reaction–diffusion systems. *Physica D: Nonlinear Phenomena*, 132(3):339–362, 1999.
- [10] S.J. Chapman and G. Kozyreff. Exponential asymptotics of localised patterns and snaking bifurcation diagrams. *Physica D*, 238(3):319–354, 2009.
- [11] J. Dawes. Localized pattern formation with a large-scale mode: Slanted snaking. *SIAM J. Appl. Dyn. Syst.*, 7(1):186–206, 2008.
- [12] J. Dawes. Modulated and localized states in a finite domain. *SIAM J. Appl. Dyn. Syst.*, 8(3):909–930, 2009.
- [13] A.D. Dean, P.C. Matthews, S.M. Cox, and J.R. King. Exponential asymptotics of homoclinic snaking. *Nonlinearity*, 24(12):3323–3351, 2011.
- [14] M. Golubitsky, J. W. Swift, and E. Knobloch. Symmetries and pattern selection in Rayleigh-Bénard convection. *Physica D: Nonlinear Phenomena*, 10(3):249–276, 1984.
- [15] M. F. Hilali, S. Métens, P. Borckmans, and G. Dewel. Pattern selection in the generalized Swift-Hohenberg model. *Phys. Rev. E*, 51:2046–2052, Mar 1995.
- [16] S. M. Houghton and E. Knobloch. Homoclinic snaking in bounded domains. *Phys.Rev.E*, 80:026210, 2009.
- [17] G. Kozyreff, P. Assemat, and S.J. Chapman. Influence of boundaries on localized patterns. *Phys. Rev. Letters*, 103:164501, 2009.
- [18] M. Leda, V. K. Vanag, and I. R. Epstein. Instabilities of a three-dimensional localized spot. *Phys. Rev. E*, 80(6):66204, 2009.
- [19] D.J.B. Lloyd, B. Sandstede, D. Avitabile, and A.R. Champneys. Localized hexagon patterns of the planar Swift-Hohenberg equation. *SIAM J. Appl. Dyn. Syst.*, 7(3):1049–1100, 2008.
- [20] J.D. Murray. *Mathematical biology*. Springer-Verlag, Berlin, 1989.
- [21] Y. Pomeau. Front motion, metastability and subcritical bifurcations in hydrodynamics. *Physica D*, 23:3–11, 1986.
- [22] H. Uecker and D. Wetzel. Numerical Results for Snaking of Patterns over Patterns in Some 2D Selkov-Schnakenberg Reaction-Diffusion Systems. *SIAM J. Appl. Dyn. Syst.*, 13(1):94–128, 2014.
- [23] H. Uecker, D. Wetzel, and J. Rademacher. pde2path – a Matlab package for continuation and bifurcation in 2D elliptic systems. *Numer. Math. Theor. Meth. Appl.*, 7(19):58–106, 2014.